

A Wireless Subdural Optical Cortical Interface Device with 768 Co-Packaged Micro-LEDs for Fluorescence Imaging and Optogenetic Stimulation

Yatin Gilhotra¹, Henry Overhauser¹, Heyu Yin¹, Eric Pollmann¹, Guy Eichler¹, Andrew Cheng¹, Taesung Jung¹, Nanyu Zeng¹, Luca P. Carloni¹, Kenneth Shepard¹

¹Columbia University, New York, NY, USA

One of the goals of neuroengineering is to establish high-bandwidth, fully implantable, and minimally invasive wireless neural interfaces that help interrogate neural circuits in freely moving and socially behaving animals. Optical interfaces offer advantages over electrophysiological techniques such as cell-type specificity, low cross-talk bidirectionality, and wide field-of-view (FoV). While most optical interfaces to-date have taken the form of bulky “mini-scopes”, recent advances in optical interfaces have shown promise in achieving high-resolution, volume-efficient brain interfacing over large FoVs with devices accommodated entirely within the subdural space [1, 2]. These devices, however, still require wired connection through the skull, negating advantages of their volumetric efficiency.

We introduce a fully wireless, 12x12 mm² subdural optical interface with a 5.76x7.68 mm² FoV for lens-less imaging and optogenetic stimulation. The FoV can span multiple brain regions in non-human primates, enabling brain coordination studies with unprecedented detail. The device features monolithically integrated single-photon avalanche diodes (SPADs) in a 192x256 array with a pitch of 30μm for fluorescence imaging, complemented by an integrated array of 24x32 micro-LEDs (μLEDs) with 240μm pitch for fluorescent excitation and optogenetic stimulation. A hybrid emission filter, an excitation filter, and a computational imaging mask complete the packaging stack-up as shown in Fig. 1. The CMOS die is thinned to approximately 15μm; the entire device is approximately 150μm thick and mechanically flexible to a radius of curvature of 12.5mm. On-chip antennas support wireless powering and bidirectional ultra-wide-band (UWB) radio link. The implant communicates with and is powered by a wearable “relay station” positioned directly outside the skull as shown in Fig. 1.

The block diagram of the implantable device fabricated in 130nm BCD technology with wireless packet structure and instruction set is shown in Fig. 2. Each pixel contains a 10-bit modulo counter for dynamic range extension with a 5% fill factor (FF). The light detectors are interleaved with 60x60μm² μLED sites, driven by individually addressable and programmable current drivers, allowing complex patterns of fluorescence excitation and optogenetic stimulation. We fabricate the custom μLED array, using GaN/InGaN active layers epitaxially grown on a double-side-polished sapphire wafer. After flip-chip bonding to the CMOS die, laser-lift-off releases the sapphire substrate, leaving a 6-μm-thick μLED film. These μLEDs have peak emission at 460nm to excite GCamp6f calcium indicators; while red μLEDs have peak emission at 640nm used to excite ChRmine opsins. Each μLED has an emission area of 80x80μm². For fluorescence excitation, the hybrid emission filter provides background rejection of 5.5 OD at 520nm as shown in Fig. 3. Blue excitation filter centered at 460nm gives 3 OD at 520nm.

The SPAD pixels in each row share a 10-bit bus and are read out serially with a 13.56-MHz clock. 1920-bit bus from 192 rows is serialized into one high-speed data channel and fed to the implant controller for packetization-depacketization of data, error correction, and the generation and decoding of synchronization bits embedded in the packet. The controller also decodes instructions, sets biasing, and configures the imager and μLED array. The controller can select partial array read-out on an active column basis allowing for trade-off between frames-per-second (fps), integration time, and the FoV of imager. The system can image at 176fps over the entire FoV, but this increases to 400fps for FoV of 5.76x3.36mm² to image faster dynamics of voltage indicators.

The controller serializes and deserializes data to the on-chip UWB transceiver, which interfaces with the external wireless relay station. This station is equipped with a dipole antenna for telemetry, a power-delivery coil and operates through a Python software interface to the

underlying implant instruction set. In the on-implant transmitter, a duty-cycled LC-VCO operates with a peak output power level of 10dBm, achieving an energy efficiency of 50pJ/bit [3]. The link uses on-off-keying (OOK) modulation with 4GHz carrier. Uplink and downlink data rates are 108Mbps and 54Mbps, facilitated by a T/R switch enabling time-division duplexing. The receiver contains an LNA, followed by a self-mixing double-balanced mixer and a Strong-Arm-style comparator for decision making, operating at 200pJ/bit. A PLL is used to derive the 108.48MHz clock from the 13.56MHz carrier.

An inductively-linked on-chip wireless power transfer system is employed to generate required voltages. A 765-nH on-chip power-coil routed in ultra-thick top metal is impedance matched to an active rectifier at 13.56MHz to generate an unregulated DC chip supply of 2V. This rectifier achieves 87% efficiency, and supports 30mA of current. The rectifier powers an LDO bank, that generates 1.5V VDD for in-pixel logic, controller, and the transceiver. For μLEDs and SPAD biasing, a single-stage charge pump (CP) and a 19-stage CP are used to generate 2.7V and 30V, respectively. The rectifier output voltage is determined by both the power-delivered by the relay-station and power-consumed on-chip. To maintain desired voltage levels, we employ a three-bit flash ADC that uses a fixed bandgap voltage as a reference to periodically monitor and adjust the on-chip rectifier output in software. To keep low-noise power-profile, the chip uses >100nF decoupling capacitance aggregated across all supplies.

Fig. 3 shows the optical characteristics of the both the SPADs and μLEDs, including the photon detection probability profile of the SPAD, the linearity of the measured illumination intensity, and the optical output power of the μLEDs as a function of current drive. At an excess bias of 2V, SPADs exhibit a peak photon-detection-probability (PDP) of 12% at 630nm and a PDP of 5% at 520nm. The blue μLEDs have peak emission at 460nm with a 10% external quantum efficiency (EQE). The use of a 10-bit modulo counter provides a dynamic range of over 70dB with a global shutter. Some pile-up non-linearity is observed in the SPAD counts, which can be corrected with calibration.

Fig. 5 shows the functional waveforms for the OOK based data-telemetry, CP unit stage, clock scheme, and rectifier design. SPAD and μLED charge-pump voltages as a function of programming code is also shown. For the case of the SPAD charge pump, the output ranges from 25.2-31.6V, and 2.6-3.1V for the case of μLED charge-pump. The SPAD charge-pump output increases with the rectifier output voltage (RECT_VDD). The μLED excitation output was found to be stable within 0.6% of nominal value while recording which allows for robust imaging of fluorescence indicators with typical contrasts of >20%. The uplink channel has a BER of less than 2.28x10⁻⁹ through 2cm of tissue phantom. The system consumes a maximum power of 60mW including 12mW for the μLEDs, keeping heating in air to less than 39C, as confirmed with a calibrated FLIR thermal imaging device. Fig. 5 compares the performance of this work with the state-of-the-art fluorescence imagers. Fig. 6 shows the monte-carlo analysis of dense μLED array which allows near uniform illumination beyond 100μm depth. The packaged CMOS + μLED array is also shown. The initial fluorescence image of clusters of Fluoresbrite YG microspheres taken wirelessly with the packaged device is compared with ground truth in the absence of computational mask. Better than 60μm resolution is expected with computational mask integration.

Acknowledgement:

This work was supported in part by DARPA under Contract N66001-17-C-4012.

References:

- [1] S. Moazeni et al., IEEE TBioCAS, vol. 15, no. 6, pp. 1295-1305, Dec. 2021.
- [2] E. H. Pollmann et al., IEEE ESSCIRC, pp. 205-208, Sep. 2022.
- [3] N. Zeng, et al., IEEE Symposium on VLSI Technology and Circuits, Jun. 2023.
- [4] E. P. Papageorgiou et al., IEEE Symposium on VLSI Circuits, Jun. 2017.
- [5] R. Rabbani et al., IEEE Custom Integrated Circuits Conference, Apr. 2022.



Die Micrograph.

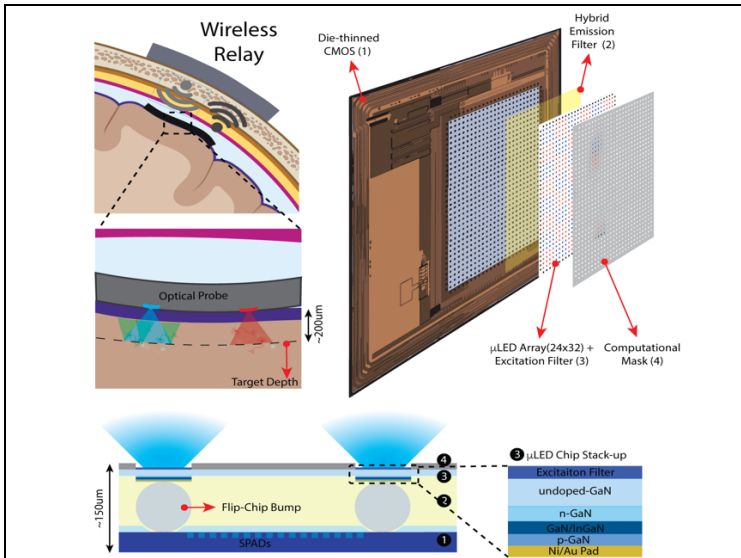


Fig. 1. Conceptual diagram of the device, the packaging scheme, and the μ LED Chip layer stack-up

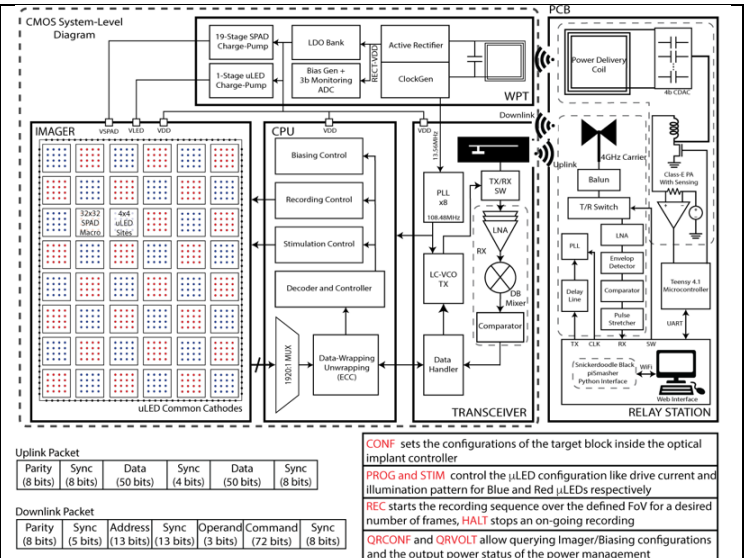


Fig. 2. System-level block diagram of the CMOS implant, the wireless relay-station, packet structure and implant instruction-set

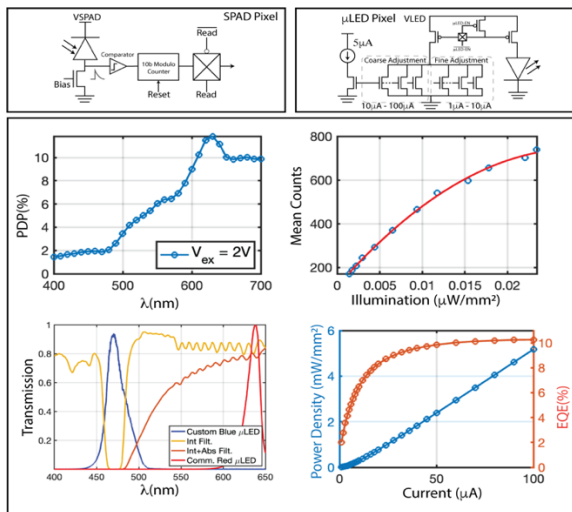


Fig. 3. SPAD pixel (top-left), μ LED pixel (top-right), SPAD PDP (%) (middle-left), SPAD linearity (middle-right), Hybrid emission filter and custom blue μ LED output spectrum (bottom-left), μ LED power density and EQE (%) with current sweep (bottom-right)

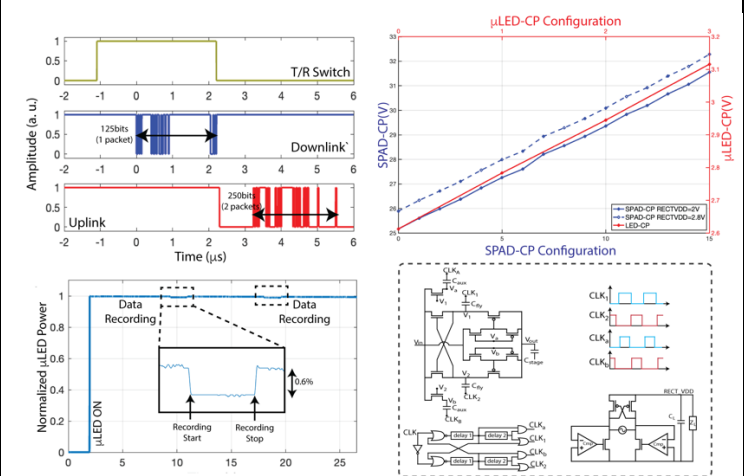


Fig. 4. Digitized data telemetry recorded at the relay-station (top-left), SPAD and μ LED charge-pump output versus programmable configuration (top-right), μ LED optical power stability with time (bottom-left), Charge-pump unit stage, clock driver and scheme, and active rectifier (bottom-right)

Parameters	[4]VLSI'17	[1]TBCAS'21	[2]ESSCIRC'22	[5]CICC'22	This Work
CMOS Technology	180nm	130nm	130nm	180nm	130nm
Supply Voltages	1.8V/5V	1.5V/1.8V/2.4V/14V	1.5V/1.8V/2.4V/18V	1V/1.8V/2.1V/2.5V/3.3V	1.5V/2V/2.7V/28.5V
FoV(mm ²)	4.7x2.25	5.4x5.4	5.1x6.8	1.98x2.2	5.76x7.68
Pixel Pitch(μ m)	55	30	25	55	30
FF/Peak-PDP(%)	28/5*(QE)	5/12	11.5/9	N/A	5/12
Dark Count(Hz)	27fA	26	17	N/A	61
Resolution(μ m)	220	60	50	140*	60
Power(mW)	3.5**	40**	18† **	0.055††	48**
Array Size	36 x 80	160 x 160	192 x 256	36 x 40	192 x 256
Frame Rate(fps)	20	125	200/400	0.006	176/400
Data Telemetry(Mbps)	N/A	40	100	0.011	TX:108.48 RX:54.24
Integrated Light Sources (Number)	No	Yes (24)	Yes (24)	Yes (1)	Yes (768)
Wireless Data	No	No	No	Yes, US-Backscatter	Yes, UW-IR
Wireless Power	No	No	No	Yes, Ultrasound	Yes, 13.56MHz Inductive
Bidirectionality	No	Yes	Yes	No	Yes

* Estimated from graphs/data, ** Illumination power not included, † Imager power not included, †† Overall system power including imaging and illumination

Fig. 5. Comparison table with the state-of-the-art fluorescence imagers

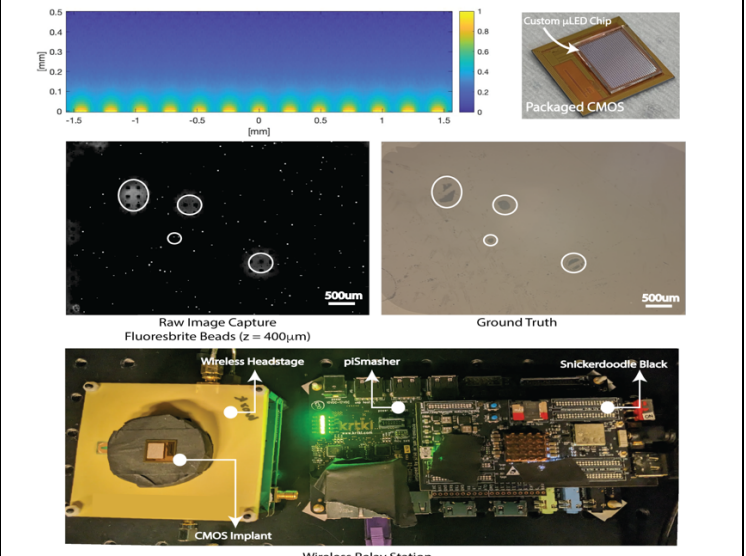


Fig. 6. Monte Carlo of μ LEDs, packaged CMOS, Image capture of wireless chip vs ground truth, and wireless relay-station hardware